Planar LTCC Transformers for High-Voltage Flyback Converters

Alexander W. Roesler, *Member, IEEE,* Joshua M. Schare, S. Jill Glass, Kevin G. Ewsuk, George Slama, David Abel, and Daryl Schofield

***Abstract*—This paper discusses the design and use of low-temperature (850 °C to 950 °C) cofired ceramic (LTCC) planar magnetic flyback transformers for applications that require conversion of a low-voltage to high-voltage (>100-V) with significant volumetric constraints. Measured performance and modeling results for multiple designs show that the LTCC flyback transformer design and construction imposes serious limitations on the achievable coupling, and significantly impacts the transformer performance and output voltage. This paper discusses the impact of various design factors that can provide improved performance by increasing transformer coupling and output voltage. The experiments performed on prototype units demonstrate LTCC transformer designs capable of greater than 2-kV output. Finally, the paper investigates the effect of the LTCC microstructure on transformer insulation. Although this paper focuses on generating voltages in the kV range, the experimental characterization and discussion presented in this paper applies to designs requiring lower voltage.**

***Index Terms*—Ceramics, dc–dc power conversion, ferrite devices, switched mode power supplies, transformer cores, transformer windings, transformers.**

I. Introduction

NUMEROUS commercial electronic systems operate by discharging a high-voltage capacitor into a load. These systems usually require the conversion of a low-voltage input to a high-voltage output across a discharge capacitor (>100-V). Examples include photographic flash (e.g., for driving xenon flashlamps in cameras and cell phones) and emergency warning beacons. The flyback topology provides a simple and cost-effective method for stepping up to high-voltage and consequently finds widespread use in these applications [1]. For the majority of these systems the transformer represents one of the largest and most expensive components. There exists a growing need for miniature, low-profile, low-cost transformers for use in these applications to support current technology trends which continually push for lower cost and size reduction. Efforts in recent years have focused on the use of low-profile magnetic core structures with printed circuit board (PCB) coils to shrink the size of the transformer used in power processing systems [2] and [3]. However, for high-voltage converter designs that require transformers with a large turns ratio and a large number of windings, the integration of the coil into the PCB structure requires multiple conductor layers in the PCB design. This can significantly increase the cost and complexity of the PCB.

This paper discusses the design of low-temperature (850 °C to 950 °C) cofired ceramic (LTCC) ferrite-based transformers for use in high-voltage flyback converter systems. LTCC ferrite combined with screen printable silver conductor and low-permeability dielectric produces small surface mountable transformers with no wire or discrete core. The LTCC transformers integrate the conductor, insulator, and magnetic materials into a single monolithic device, leading to size reduction and a very low profile. This approach provides automated, parallel transformer manufacturing which supports low-component cost.

While this paper focuses on flyback transformer designs, the concepts presented can also be extended to other transformer and inductor applications. The designs and processing approaches discussed also lend themselves to integration of ferrite transformers with other LTCC packaging materials.

Manuscript received February 2, 2009; revised August 6, 2009. Date of publication October 30, 2009; date of current version June 9, 2010. Sandia is a multiprogram laboratory operated by Sandia Corporation, a Lockheed Martin Company, for the United States Department of Energy's National Nuclear Security Administration under Contract DE-AC04-94AL85000. Recommended for publication by Associate Editor J. E. Morris upon evaluation of reviewers' comments.

A. W. Roesler, J. M. Schare, S. J. Glass, and K. G. Ewsuk are with Sandia National Laboratories, Albuquerque, NM 87123-3453 USA (e-mail: awroesl@sandia.gov; jmschar@sandia.gov; sjglass@sandia.gov; kgewsuk@sandia.gov).

G. Slama, D. Abel, and D. Schofield are with NASCENTechnology, Watertown, SD 57201 USA (e-mail: gslama@nascentechnology.com; dabel@nascentechnology.com; dschofield@nascentechnology.com).

Color versions of one or more of the figures in this paper are available online at http://ieeexplore.ieee.org.

Digital Object Identifier 10.1109/TCAPT.2009.2031872

II. Background on Flyback Converters

Fig. 1 shows the basic flyback converter circuit assuming an ideal transformer. During the time interval when the gate drive turns the switching metal–oxide–semiconductor field-effect transistor (MOSFET) on, current flows only through the primary since the diode prevents current flow in the secondary winding. This results in stored energy on the primary during the time interval that the MOSFET conducts. The amount of energy stored depends on the peak current in the primary (I_{pk}) before the switch turns off, as determined by the drive voltage V_{in}, primary inductance L_p and turn on time t_{on} of the switch

$$I_{pk} = \frac{V_{\text{in}}}{L_p} t_{\text{on}}. \tag{1}$$

When the MOSFET switch turns off the current flow through the primary winding, the mutual coupling of the transformer

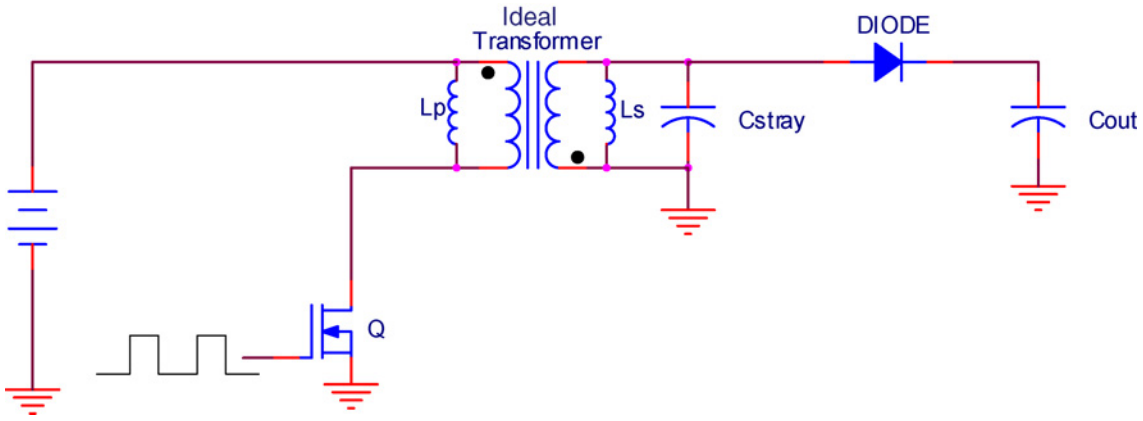

Fig. 1. Flyback converter circuit schematic assuming an ideal transformer.

transfers the stored energy to the secondary. Since the current in an inductor cannot change instantaneously, the current on the primary transfers to the secondary. The resulting current flows through the diode and generates a voltage drop across the output capacitor. The total voltage across the capacitor increases each switching cycle until it reaches a maximum limited by the transformer output capabilities (assuming the circuit runs without feedback regulation as shown in Fig. 1). For a given flyback transformer design, energy transfer to the secondary stray capacitance governs the maximum achievable output voltage

$$E_p = \frac{1}{2}L_p I_p^2 = \frac{1}{2}C_{\text{stray}}V_{\text{out}}^2 = E_s \Rightarrow V_{\text{out}} = I_p\sqrt{\frac{L_p}{C_{\text{stray}}}} \quad (2)$$

where I_p is the primary current, C_{stray} is the secondary stray capacitance, E_p is the energy stored on the primary, E_s is the energy stored on the secondary and V_{out} is the output voltage across the secondary load.

Fig. 2 provides theoretical primary current and output voltage waveforms for the simple flyback circuit shown in Fig. 1. Note that the present paper focuses only on the discontinuous mode of operation, in which all energy transfers to the load during the off time of each switching cycle before the switch turns on again. This energy transfer is evident by the leveling of V_{out} during the MOSFET off time in Fig. 2.

The preceding analysis assumes an ideal transformer and ignores the effects of leakage inductance on the circuit. For a transformer the total primary inductance actually consists of two components (Fig. 3): 1) the component which creates a flux that links the secondary, termed the magnetizing inductance, L_{mp}, and 2) the component which creates a flux that links only the primary, termed the leakage inductance, L_{lp}. The leakage inductance decreases overall efficiency since the energy stored in the leakage inductance does not transfer to the secondary when the switch turns off [4]. Only the primary magnetizing inductance

$$L_{mp} = L_p - L_{lp} \quad (3)$$

contributes to the transferred energy. The coupling coefficient, k, of the transformer provides a relationship between the

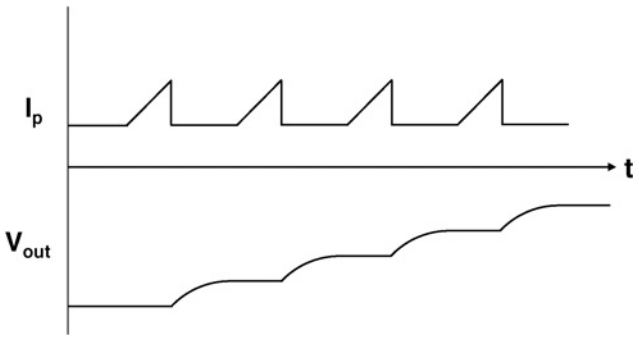

Fig. 2. Waveforms showing theoretical operation of the flyback converter. During the time the switch conducts, the current ramps linearly through the primary. When the switch turns off, energy transfers to the secondary and increases the voltage across the output capacitor.

leakage and magnetizing inductances, and is defined in this article as

$$k = \sqrt{\frac{L_p - L_{lp}}{L_p}} = \sqrt{\frac{L_{mp}}{L_p}}. \quad (4)$$

Perfect coupling results in a value of unity for the coupling coefficient.

Substituting magnetizing inductance in place of primary inductance in (2) provides a relationship between the maximum achievable output and the coupling coefficient

$$V_{\text{out}} = I_p\sqrt{\frac{L_{mp}}{C_{\text{stray}}}} = kI_p\sqrt{\frac{L_p}{C_{\text{stray}}}}. \quad (5)$$

Additionally, note that only the flux that links the secondary contributes to the mutual inductance, M, of the flyback transformer

$$M = NL_{mp} = k^2NL_p \quad (6)$$

where N is the ratio of secondary to primary turns (i.e., the transformer turns ratio). This leads to the definition of an effective turns ratio for the transformer

$$N_{\text{eff}} = k^2N. \quad (7)$$

Besides degrading efficiency, the leakage inductance also impacts overall operation and performance of the converter

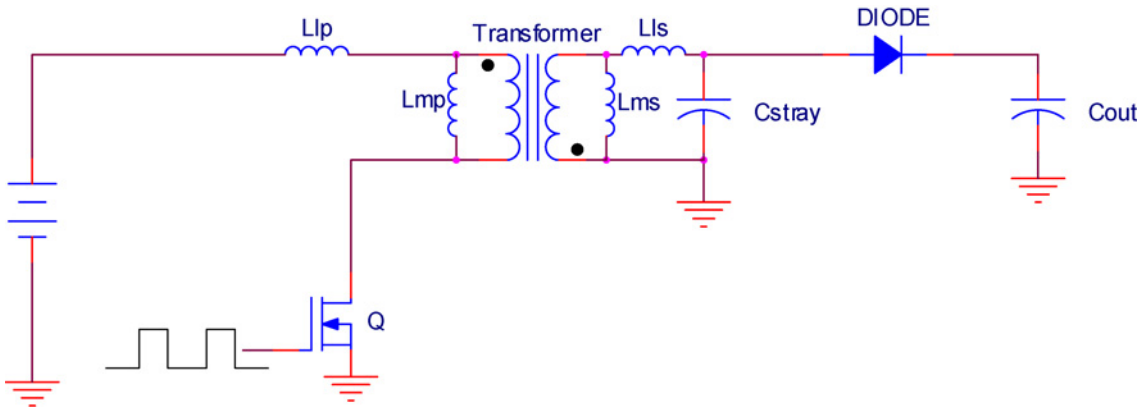

Fig. 3. Flyback converter circuit schematic that includes effects of leakage inductance.

circuit. Unlike the primary magnetizing inductance, no alternative path exists for the leakage inductance current when the switch turns off (recall that the magnetizing current transfers to the secondary when the switch turns off). Instead, current in the leakage inductance continues to flow since current through an inductor cannot change instantaneously. In other words, the leakage inductance behaves as an unclamped inductive load when the switch turns off. The charge that continues to flow after the switch turns off accumulates onto the parasitic elements in the transformer and the switch. This creates a sharp voltage spike on the drain of the MOSFET with a magnitude determined by the parasitic elements and the energy stored in the leakage inductance. The voltage spike adds to the input voltage and reflected output voltage, leading to a total peak voltage on the drain of the switch given by [4]

$$V_{\text{dss}} = V_{\text{in}} + \frac{V_{\text{out}}}{N_{\text{eff}}} + I_p \sqrt{\frac{L_{lp}}{C_p + C_{\text{oss}}}} \tag{8}$$

where V_{in} is the input voltage, C_p is primary winding capacitance in the transformer, and C_{oss} is the output capacitance of the MOSFET.

Snubber circuits can be used to suppress the voltage spike [4]. However, they are not utilized in this paper. Details of the experimental setup are provided later in this paper.

III. Background on LTCC Transformer Construction

LTCC is a well-established process that has been in use for many years in the microelectronics packaging industry. The process for building transformers uses a ferrite-based green tape prepared from a slurry of ceramic oxides, plasticizers, binders, and solvents. The slurry is cast onto a mylar carrier film moving under a knife-edge, the height of which determines the tape thickness. Air drying the slurry removes the solvent and allows the formation of the tape—which is only a few tens of micrometers (μm) thick.

The tape is then cut into sheets that become the individual layers of an assembly, called a "stack." A single sheet may be large enough to contain a matrix of hundreds of transformers, similar to integrated circuit wafers. The sheets are

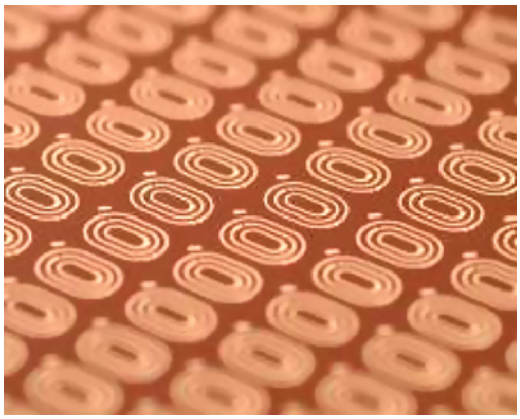

Fig. 4. Screen printed conductive coils for a 1:2 transformer design on a ferrite sheet.

punched with a series of holes for both tooling alignment and for via interconnections between layers. Vias are then filled with a conductive material using a stencil and screening process. The next step involves screen printing conductive patterns onto each sheet that represent the windings and interconnecting traces. Fig. 4 provides an illustration of a sheet with printed conductor windings for a 1:2 transformer design.

The next and final printing applies a low-permeability material to selected areas, creating a magnetic path structure critical to the transformer performance [5]–[7]. Later discussion will illustrate the effects of this dielectric layer on performance. Fig. 5 provides an illustration of one of the coils in Fig. 4 after screen printing the low-permeability dielectric.

The sheets are then aligned and stacked together. High-pressure pressing, or laminating, melds all the layers into a solid mass. The matrix of transformers is then singulated into individual pieces. Next, they are fired in a furnace following a precise and carefully controlled temperature profile with peak temperatures in excess of 800 °C. The firing process burns off the organic binders and plasticizers, and then sinters the layers and printings into a solid monolithic structure, physically bonding the particles together. Unless there are

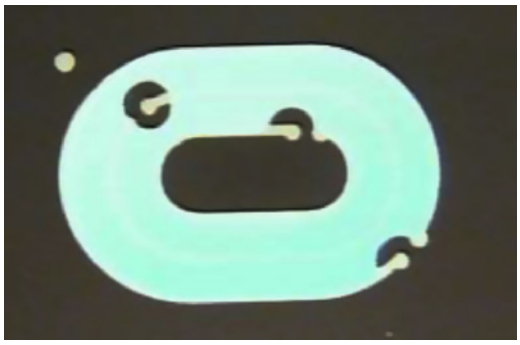

Fig. 5. Highlight of a transformer winding after applying a low-permeability dielectric.

special termination requirements, the parts are complete and ready for testing, packaging, and shipment.

As mentioned previously, the transformer processing includes the addition of a low-permeability dielectric to the transformer structure. Without the low-permeability dielectric, upon firing the coils become completely embedded in ferrite with uniform permeability throughout. This results in very poor coupling and extremely poor transformer performance. Fig. 6 provides an illustration from a finite element method magnetics (FEMM) finite element model [8] that shows the flux distribution in an LTCC transformer without the low-permeability layers. (The figure shows a 2-D axisymmetric cross-section for one half of the transformer.) Note that the design possesses an interleaved winding structure (primary sandwiched between secondary windings) and an 8:1 turns ratio. The image clearly shows the poor flux linkage with the secondary, with a large portion of the flux traveling through the regions of the transformer that contain the secondary windings. The inclusion of the low-permeability layer over each winding layer creates a higher reluctance magnetic path through the winding regions. The flux therefore prefers the low-reluctance core path, thereby leading to a considerable improvement in the coupling. Fig. 7 provides FEMM output for the same transformer in Fig. 6, with the low-permeability layers. The structure possesses noticeably improved coupling.

Similar to the formation of the high-reluctance path through the windings regions, the low-permeability dielectric can also provide a method for incorporating a high-reluctance path through the core. This provides the same benefits as adding an air gap to a conventional wirewound flyback transformer; namely, it prolongs the onset of saturation and allows for increased energy storage. In the case of the LTCC transformer, the gaps are completely monolithic and embedded between the ferrite tape layers. All of the designs discussed in this article include monolithic dielectric gapped cores, and subsequent sections will illustrate the effect of the gap on performance. Note that relatively minor differences in the dielectric print thickness for a build can impact final inductance of the design since the cumulative effect on multiple layers alters the transformer reluctance. Consequently, inductance can vary from one lot build to another. This should be kept in mind for the results presented in this paper.

IV. Experimental and Modeling Setup

Fig. 8 provides an electrical schematic showing the circuit used to test the output performance of the LTCC transformers. All output voltage measurements utilized a 100:1 resistive divider. The reported transformer output voltages in the article correspond to the peak voltage measured across a 0.1 μF output capacitor with a 15-V input voltage and a 50 kHz switching frequency. Note that an oscilloscope was utilized to determine the peak output voltage achieved across the capacitor. The MAX4427 MOSFET driver translates the HP8112A function generator output to a high-voltage/current output for efficiently turning the IRF740 MOSFET on and off. All experiments operated with no feedback regulation in order to determine the maximum output capability for the transformer.

For basic parameter testing, all inductance measurements were performed using a Wayne Kerr PM3260B Precision Magnetics Analyzer set to 100 kHz, 100-mV. The leakage inductance, L_{lp}, represents the inductance measured across the primary with the secondary windings shorted. A Valhala Scientific 4014 Digital Ohmmeter provided all winding resistance measurements.

All reported simulation results used the FEMM software [8]. FEMM uses a 2-D solver, and each model assumed axial symmetry (i.e., a circular winding). Correspondingly, the models only calculate the flux distribution in one half of the transformer. For transformer cores with elliptical or "stretched" windings, the winding and core radii used in the model were set to the average of the radius length and radius width from the final physical dimensions.

V. LTCC Transformer Designs

For this effort four LTCC transformer designs were built and tested. Each design used the same base materials for its construction. For the ferrite, the 40012-28J magnetic tape produced by ESL ElectroScience was used. This tape provides a final relative permeability >450 (at 100 kHz) when cofired into transformers with the conductor and dielectric materials. The transformers also utilized ESL ElectroScience's 4926-RJ series dielectric paste for the low-permeability dielectric. Finally, all windings (primary and secondary) were formed using ESL ElectroScience's 903-CT-1J screen-printable silver conductor paste, and ESL ElectroScience's 902-J paste was used for filling vias.

The designs consist of two different winding structures: 1) one with the primary outside of the secondary windings, as shown on the left side of Fig. 9, and 2) an interleaved structure with the primary sandwiched between the secondary windings, as shown on the right side of the winding structures illustrated in Fig. 9 (in the middle of Fig. 9). The top left design, referred to as the D47 transformer, measured 9.144 mm width, 9.906 mm length and approximately 2.032 mm height. The top right winding design, referred to as the D50E transformer, possessed similar dimensions. Both the D47 and D50E designs contained stretched windings to maximize their core area. The bottom two winding designs, referred to as the D48A and D48B designs, possessed final dimensions of 7.62 mm width, 7.62 mm length and 2.032 mm height. All of the transformer

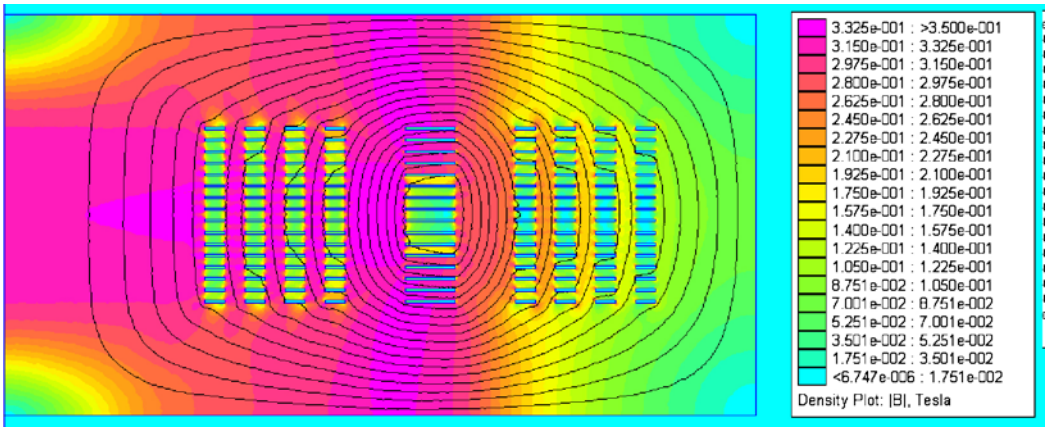

Fig. 6. Output from a FEMM model showing poor coupling for an LTCC transformer without low-permeability dielectric over the winding layers. A large portion of the flux traverses through the secondary windings. The primary current was set to 1 A in the model.

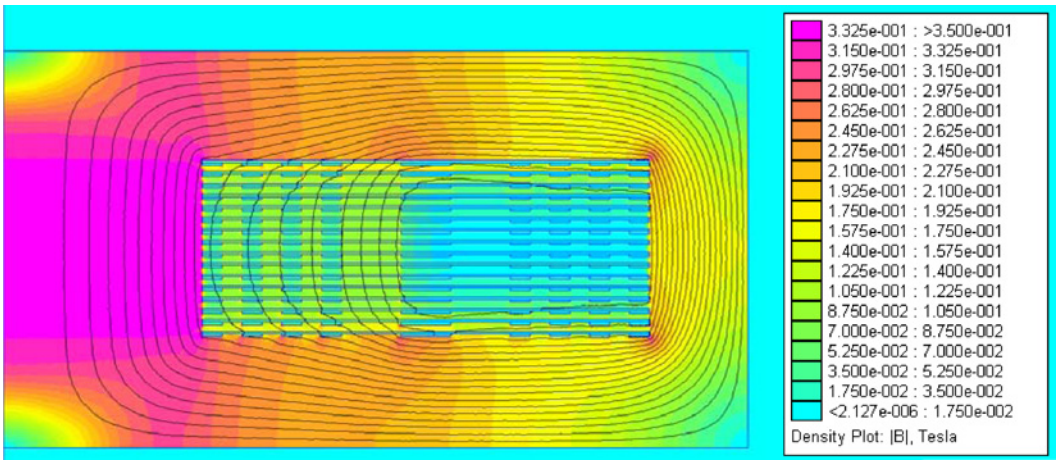

Fig. 7. Output from a FEMM model showing the improved coupling obtained when including a low-permeability dielectric layer on top of each winding print. The dielectric layers channel the flux to the center core area. The primary current was set to 1 A in the model.

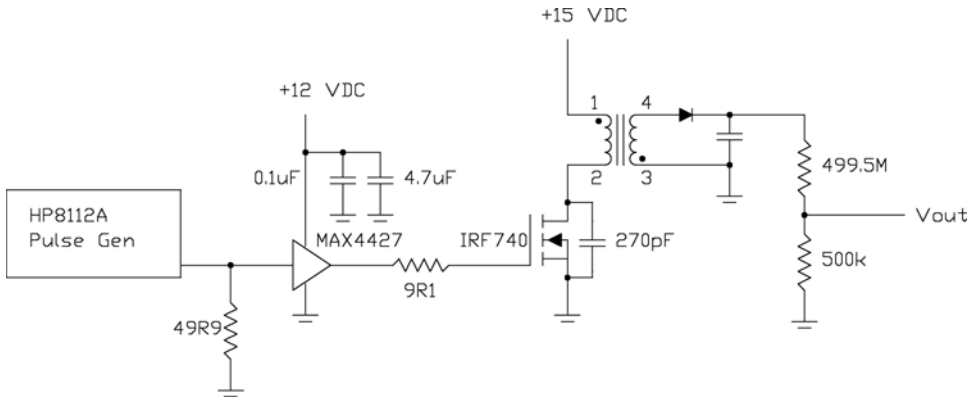

Fig. 8. Circuit schematic of the experimental setup for testing high-voltage output.

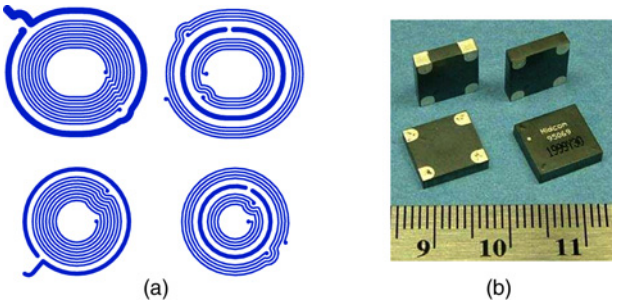

Fig. 9. (a) Winding structures for the developed LTCC transformers. Clockwise from upper left: D47 design, D50E design, D48B design, and D48A design. (b) Picture of finished D47 transformers.

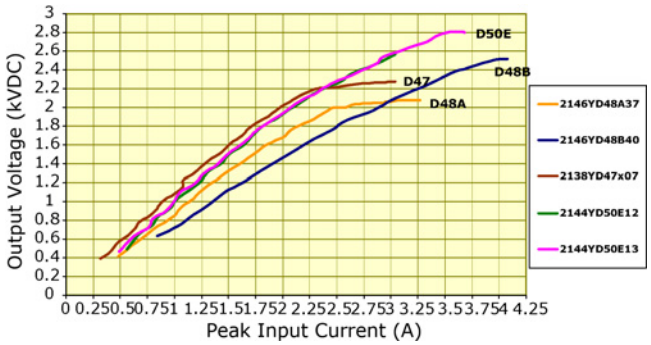

Fig. 10. Output voltage versus peak primary input current for the designs summarized in Tables I and II.

designs possess an 8:1 turns ratio, except the D47 (upper left) which possesses an 8.5:1 ratio. Table I summarizes the transformer physical dimensions and also provides information regarding the primary and secondary trace widths, primary to secondary spacing, and total number of turns for each winding. The table also lists the edge margin, defined as the space between the outermost winding and the edge of the singulated part. The shortest distance from the center of the part to the first winding is referred to as the core radius, and the stretch defines the increase in the core diameter along the orthogonal direction for the D47 and D50E designs. The right side of Fig. 9 contains a picture of finished D47 transformers.

VI. Results and Discussion

A. Impact of Transformer Design on Performance

Table II provides basic parameter data for the transformer designs highlighted in Fig. 9 and Table II, and also includes additional information about the transformer construction. The number of windings N_W refers to the total number of winding layers (Fig. 9) stacked in the transformer. The number of gaps N_G refers to the number of low-permeability dielectric gaps contained in the center core area. Note that all of the dielectric gaps are placed on the centermost tape layers in the designs. All of the designs possess relatively poor coupling and a large primary leakage inductance. This occurs because the transformer structure consists of windings possessing a

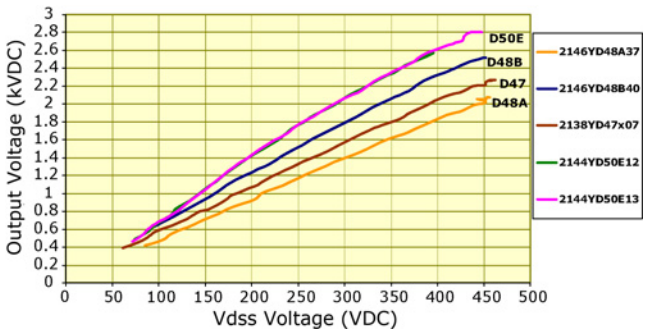

Fig. 11. Output voltage versus peak voltage across the MOSFET drain and source for the designs summarized in Tables I and II.

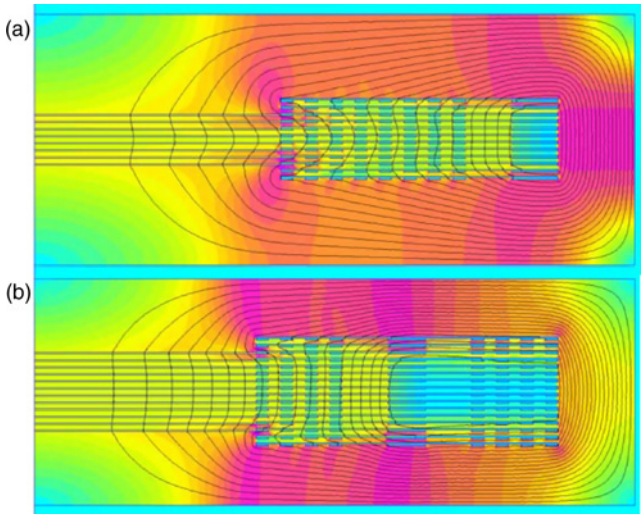

Fig. 12. FEMM plots showing field contours for (a) D47 and (b) D50E designs at 1.5 A magnetizing current.

relatively low-reluctance path, even with the addition of the low-permeability dielectric over the windings. The interleaved designs possessed higher coupling and lower leakage inductance, a benefit that this coil geometry also provides when used for wirewound transformers. Modeling results and discussion in other parts of this paper will provide further insight into the coupling characteristics of the LTCC transformer.

Fig. 10 shows the peak voltage achieved across the output capacitor at different peak current levels through the primary for each of the four designs. (In the chart, the first five digits in the legend refer to the transformer build panel number, an identifier used for tracking process parameters and materials used during fabrication of the parts. Other portions of this paper will also reference the panel number. The last two digits identify location of the part on the panel prior to singulation.) Note that the switch turn on time controls the peak current level per (1). Despite the poor coupling, all of the designs provided peak output voltages in excess of 2-kV, with the maximum output of 2.8-kV provided by the D50E transformer. The D48A and D47 designs possessed much higher primary inductance and generated higher output voltage at lower currents, as expected based on the relationship between primary inductance and output voltage shown in

TABLE I
WINDING AND DIMENSION PARAMETER DATA FOR THE DEVELOPED TRANSFORMERS (FIG. 9)

Dimensions	Units	D47	D48A	D48B	D50E
Core radius	mm	1.4478	1.2192	1.016	1.4478
Core stretch	mm	0.762	0.00	0	0.762
Length	mm	9.906	7.62	7.62	9.906
Width	mm	9.144	7.62	7.62	9.144
Height	mm	2.032	2.032	2.032	2.032
Primary turns	–	12	16	16	16
Secondary turns	–	102	128	128	128
n (N_s/N_p)	–	8.5	8:1	8:1	8:1
Wdg configuration (inner to outer)	–	8s:1p	8s:1p	4s:1p:4s	4s:1p:4s
Primary trace width	mm	0.381	0.254	0.254	0.3048
Secondary trace width	mm	0.1016	0.1016	0.1016	0.1016
Secondary trace spacing	mm	0.1016	0.1016	0.1016	0.1016
Primary–secondary spacing	mm	0.381	0.3048	0.3048	0.381
Edge margin	mm	0.635	0.508	0.508	0.635

(5). Despite their lower inductance, the interleaved designs (D48B and D50E) achieved higher peak output than the other two transformer designs, albeit at higher current levels. This occurs for two fundamental reasons. First, as shown in (5), the higher coupling for these designs allows more energy transfer to the secondary and hence higher output voltage. However, the coupling coefficients shown in Table II do not completely explain the large output difference observed on these transformers.

Understanding the output voltage performance also requires consideration of the flyback circuit operation. Equations (7) and (8) show that the coupling and leakage inductance impact the voltage stress V_{dss} across the MOSFET when the switch turns off. Fig. 11 shows the output voltage for each transformer design versus the peak voltage appearing across the switch during the off time of each switching cycle. All four designs show an increase in output voltage until the voltage across the switch reaches 450-V. At this point the voltage generated across the switch exceeds the maximum V_{dss} rating (400-V for the IRF740) and the MOSFET suffers an avalanche breakdown. This effectively clamps the output across the secondary for any further increase in the primary current, as evident in Fig. 10. Correspondingly, the output voltages in Fig. 10 represent the maximum achievable output for the different transformer designs *when utilized in the setup shown in Fig. 8.* Note that the large V_{dss} voltages result from the high-leakage inductance of these transformers. As expected from (5) and (8), designs with higher coupling (D48B and D50E) achieve a higher output voltage before reaching the V_{dss} limitation of the switch. During the experiments the primary current was monitored and never showed any evidence of transformer saturation. This suggests all four transformer designs can achieve higher output voltage when using a MOSFET with a larger V_{dss} rating.

As mentioned previously, the designs with an interleaved primary provide higher coupling and hence lower leakage inductance. Fig. 12 provides output contour plots from FEMM models that compare the D47 design and the D50E design at the same primary input current of 1.5 A. The plots show that the secondary windings located inside the primary winding create a large leakage path for the flux. Recall that the transformer construction uses the same low-permeability dielectric material for both the "gaps" located in the center core area and the high-reluctance layers deposited on top of the windings. Consequently, the center core region and the secondary windings region possess a similar reluctance. This results in the high-leakage through the secondary windings located inside the primary windings. Since the interleaved structure possesses fewer secondary windings located inside the primary winding, less flux leaks through this region. Additionally, for the interleaved structure the flux path outside the primary winding favors the low-reluctance outer edge (which contains no low-permeability material) over the higher reluctance windings region. This improves the flux linkage with the secondary. Fig. 13 shows the flux density along the centerline of the part from the same models (the centerline runs from the center of the part out radially to the edge of the part), which further illustrates the significantly improved coupling for the interleaved parts.

Fig. 14 plots the primary inductance of the D48A, D48B, and D50E designs versus the primary winding radius (for the stretched D50E design, the radius is the average along the horizontal and vertical axes in Fig. 9). Note that these three designs possessed the same number of winding, gap, and tape layers. The inductance scales linearly with the primary winding radius. This results since the flux sees a similar reluctance path inside the primary winding for these designs whether it travels through the center core or the windings region (Fig. 12). Note that this relationship will only occur when the center core contains several dielectric "gaps." Without the gaps, or with only a few gaps, the center core region will possess a much lower reluctance than the windings region. This results in a higher primary inductance that scales with the center core radius (instead of the primary winding radius). In fact, LTCC transformer designs without gaps in the center core area also exhibit much higher coupling since the flux prefers the low-reluctance core over the windings region. A comparison of Fig. 7 with Fig. 12 illustrates this effect.

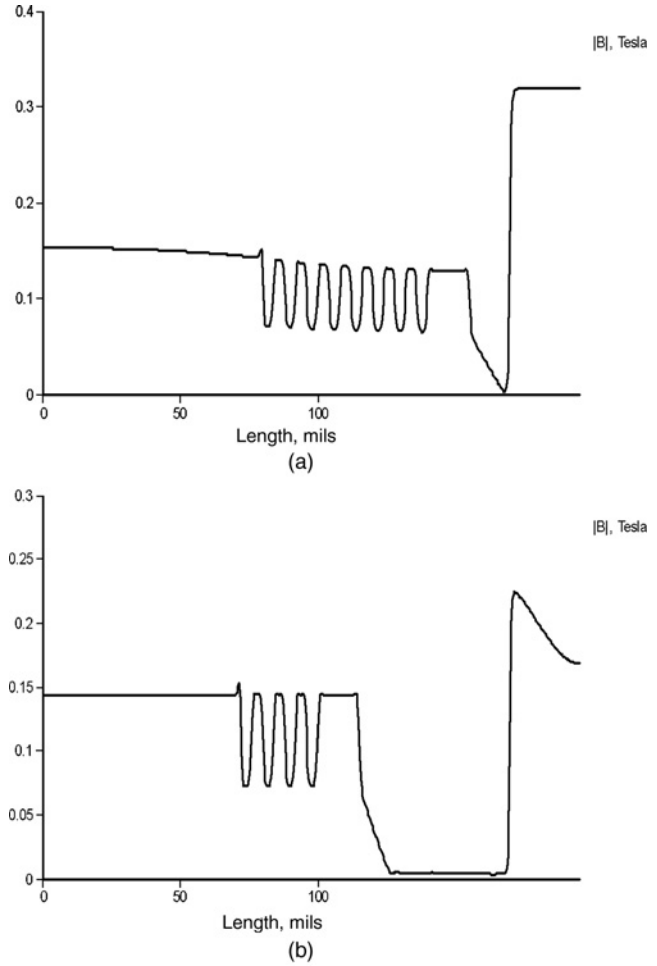

Fig. 13. Plots showing flux density along the transformer centerline for (a) D47 and (b) D50E designs at 1.5 A magnetizing current. Note that the x-axis units are in mils (0.001 in = 25.4 μm).

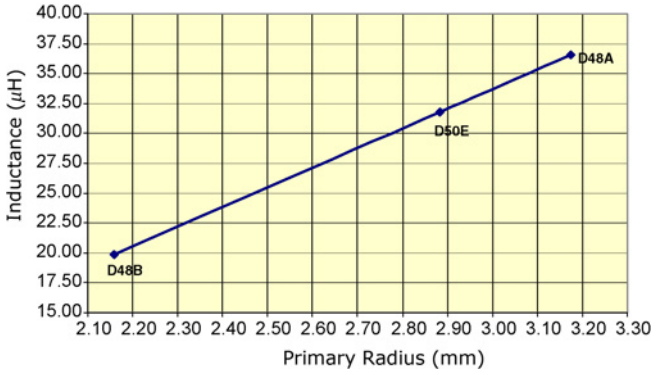

Fig. 14. Primary inductance plotted as a function of the primary winding radius.

Unfortunately, the ungapped LTCC transformers saturate at low-magnetizing currents and, therefore, provide poor flyback performance.

Referring to Table II, the D47 and D50E parts show higher coupling than the D48A and D48B designs, respectively. As the primary winding radius increases for the two different

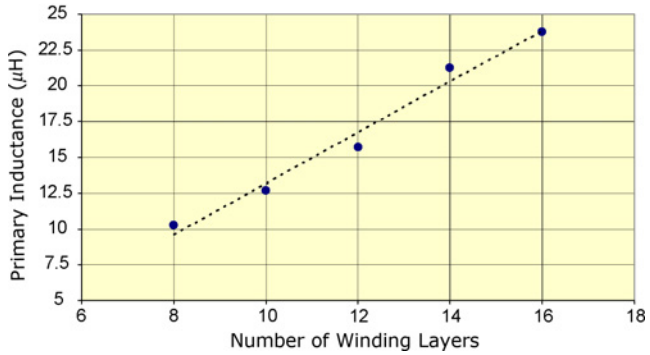

Fig. 15. Primary inductance plotted versus number of winding layers for the D48B designs summarized in Table III.

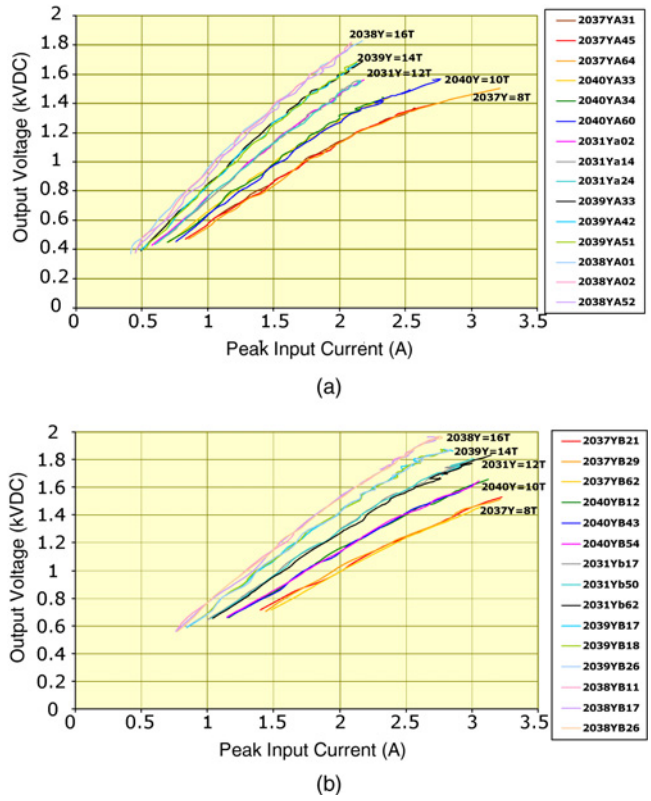

Fig. 16. Output voltage versus peak primary current for (a) D48A and (b) D48B designs summarized in Table III.

design structures shown in Fig. 9 (8s:1p and 4s:1p:4s), the ratio of the center core area to total area inside the primary winding increases. Therefore, the reluctance of the center core region decreases relative to the reluctance of the winding region. Consequently, more flux links the secondary for the designs with a larger primary radius, leading to a higher value for the coupling coefficient k.

B. Impact of Winding Structure on Performance

The LTCC transformer design incorporates multiple layers that contain the transformer windings (such as those shown in Fig. 9). The number of turns for the primary and secondary can be controlled by adjusting the number of these layers included

TABLE II

BASIC PARAMETER DATA FOR THE FOUR EXPERIMENTAL TRANSFORMER DESIGNS

Parameter	Units	D47R1	D48A	D48B	D50E
Primary inductance, L_p	μH	47.79	36.57	19.88	31.80
Primary leakage, L_{lp}	μH	20.53	16.28	6.09	8.00
Secondary inductance, L_s	μH	1550.00	930.14	893.40	1530.00
Primary resistance, R_p	Ω	1.11	1.86	1.32	1.47
Secondary resistance, R_s	Ω	21.34	24.01	26.38	35.44
Coupling coefficient, k	–	0.755	0.745	0.833	0.865
Number of tape layers, L	–	35	35	35	35
Number of gaps, N_G	–	8	12	12	12
Number of windings, N_W	–	12	16	16	16

TABLE III

BASIC PARAMETER AND BUILD DATA FOR THE D48 TRANSFORMERS USED TO INVESTIGATE THE IMPACT OF WINDING STRUCTURE ON PERFORMANCE

Parameter	Units	2037Y	2040Y	2031Y	2039Y	2038Y
Primary inductance, L_p	μH	10.28	12.70	15.69	21.23	23.77
Primary leakage, L_{lp}	μH	3.53	4.13	4.43	5.79	6.90
Secondary inductance, L_s	μH	446.00	551.86	725.75	990.00	1060.00
Primary resistance, R_p	Ω	0.84	1.03	0.97	1.40	1.60
Secondary resistance, R_s	Ω	14.90	19.31	19.26	26.86	30.82
Coupling coefficient, k	–	0.810	0.821	0.847	0.853	0.842
Number of tape layers, L	–	31	31	31	33	35
Number of gaps, N_G	–	6	8	8	10	12
Number of windings, N_W	–	8	10	12	14	16

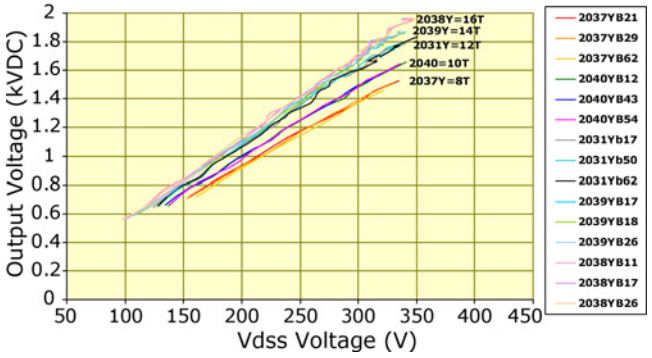

Fig. 17. Output voltage versus peak voltage across the MOSFET drain and source for the D48B designs summarized in Table III.

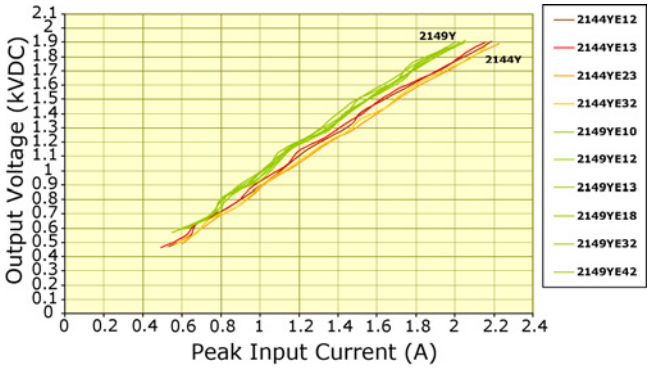

Fig. 18. Output voltage versus peak primary current for the D50E transformer designs summarized in Table V.

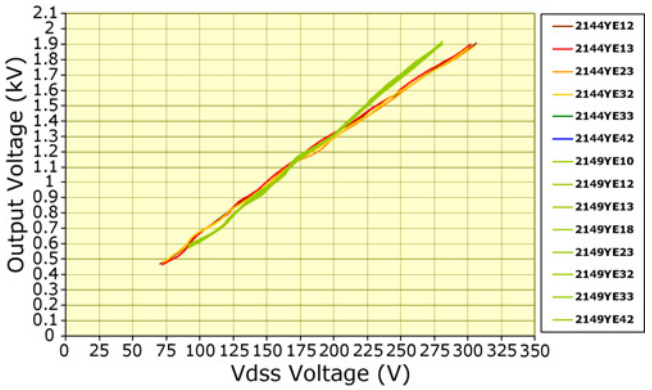

Fig. 19. Output voltage versus peak voltage across the MOSFET drain and source for the D50E transformer designs summarized in Table V.

in the final part stack-up. To better understand how this may impact transformer performance, a number of D48 transformer designs were built which varied the number of tape layers (L), number of winding layers (N_W), and number of gap layers (N_G). Table III includes the parameter data for each design. All the inductance and resistance values increase as the number of windings layers increased, an expected result.

Fig. 15 plots the primary inductance versus the number of windings layers for the fabricated D48B designs. As evident in the figure, the primary inductance shows a roughly linear relationship with the number of winding layers. (Note that the number of gap layers and the number of tape layers also change between the designs.) The primary inductance depends on the number of primary turns, N_p, and the transformer

TABLE IV
BUILD AND PARAMETER DATA FOR THE D48B DESIGN USED TO STUDY THE IMPACT OF GAP STRUCTURE ON PERFORMANCE

Parameter	Units	2030Y	2031Y	2032Y
Primary inductance, L_p	μH	19.37	16.75	17.13
Primary leakage, L_{lp}	μH	5.00	4.81	4.99
Secondary inductance, L_s	μH	915.29	754.71	765.00
Primary resistance, R_p	Ω	0.96	0.95	0.95
Coupling coefficient, k	–	0.861	0.844	0.842
Number of tape layers, L	–	31	31	31
Number of gaps, N_G	–	6	8	10
Number of windings, N_W	–	12	12	12

TABLE V
BUILD AND PARAMETER DATA FOR THE D50E TRANSFORMERS USED TO STUDY THE IMPACT OF ENDCAP STRUCTURE ON PERFORMANCE

Parameter	Units	2149Y	2144Y
Primary inductance, L_p	μH	37.22	31.80
Primary leakage, L_{lp}	μH	7.95	8.00
Secondary inductance, L_s	μH	1820.00	1530.00
Primary resistance, R_p	Ω	1.39	1.47
Coupling coefficient, k	–	0.887	0.865
Number of gaps, N_G	–	12	12
Number of windings, N_W	–	16	16
Number of layers, L	–	39	35

primary reluctance, $\Re_p$

$$L_p = \frac{N_p^2}{\Re_p}. \tag{9}$$

Since the transformer structure incorporates a low-reluctance dielectric over each winding layer as well as in the center core area, increasing the number of winding and dielectric gap layers results in a linearly proportional increase to the transformer primary reluctance. Consequently, from (9) the primary inductance varies linearly with the number of windings layers in the design.

Referring to Table III, increasing the number of winding layers shows a positive impact on coupling for the designs with the fewest winding layers, but no coupling improvement was achieved beyond 12 winding layers. Fig. 16 shows the impact of the different designs on output voltage performance for both the D48A and D48B designs. Increasing the number of windings layers provides higher output at a given primary current, as expected based on the relationship between primary inductance and output voltage shown in (5). Increasing the number of winding layers also reduced the voltage stress on the switch, as shown in Fig. 17 for the D48B designs. The reduced voltage stress was much more pronounced for the parts with fewer than 14 winding layers since the coupling of these parts showed a clear dependence on the number of winding layers. Overall, increasing the number of winding layers in the design provides a mechanism for increasing output and reducing voltage stress. This benefit should be weighed against the increased cost and more difficult processing associated with these design changes.

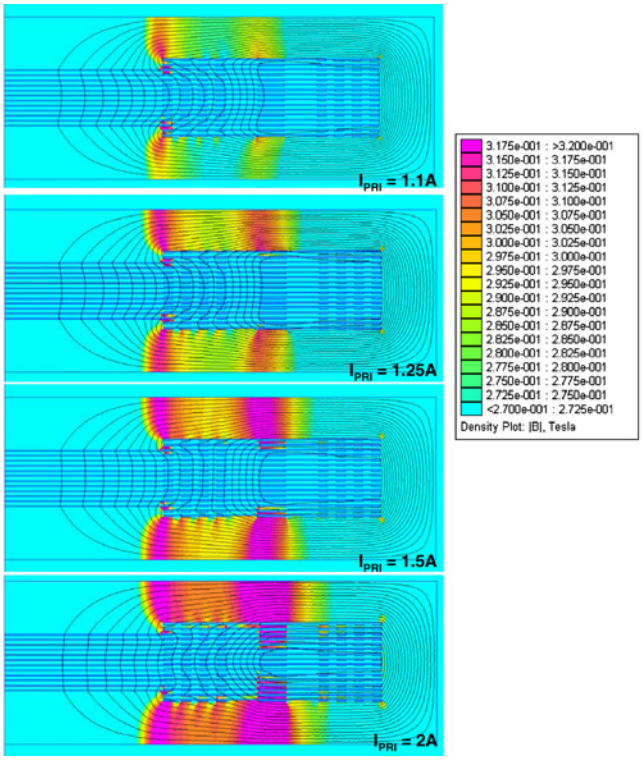

Fig. 20. FEMM contour plots for the 2144Y D50E transformer design summarized in Table V, at different magnetizing currents. The contour scale has been adjusted to make saturated regions more visible.

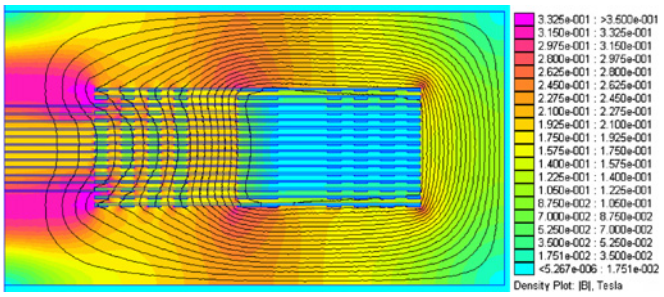

Fig. 21. FEMM contour plot for the D48B design at 2 A primary current. This design saturates in the center core area and not in the endcap regions.

C. Impact of Gap Structure on Performance

This paper also investigated the impact of the low-permeability dielectric gap structure on the transformer performance. Table IV summarizes the D48B designs used to study this effect. The designs varied the number of gaps located in the center core area, with all other variables held constant. Note that all of the gaps were placed on the centermost tape layers in the design. Table IV shows a slightly larger primary inductance for the design with six gap layers, but relatively little difference for 8 and 10 gap layers. (Recall that the LTCC transformers can exhibit variability from lot to lot, especially for differences in the dielectric print thickness. The inductance for the 8 and 10 gap designs falls within normal variation.) As discussed previously and shown in Fig. 12, the transformer reluctance depends primarily on the area inside the primary winding, i.e., the parallel combination of the

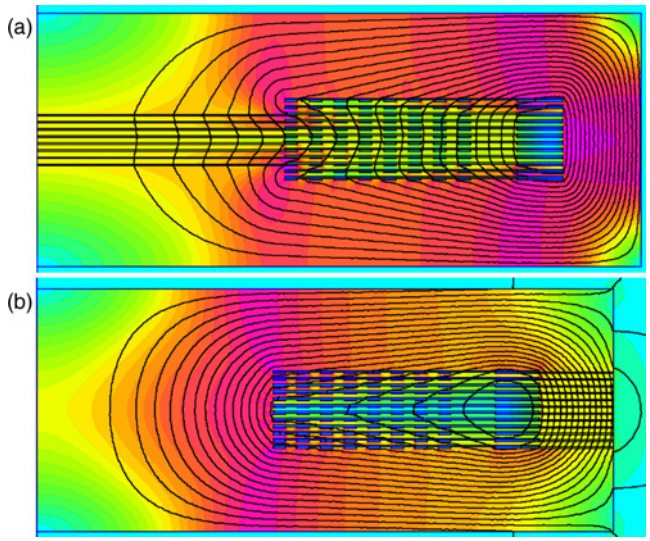

Fig. 22. FEMM contour plots showing a comparison of the D47 design with (a) center gaps and (b) edge gaps. Both images are at 2 A primary current.

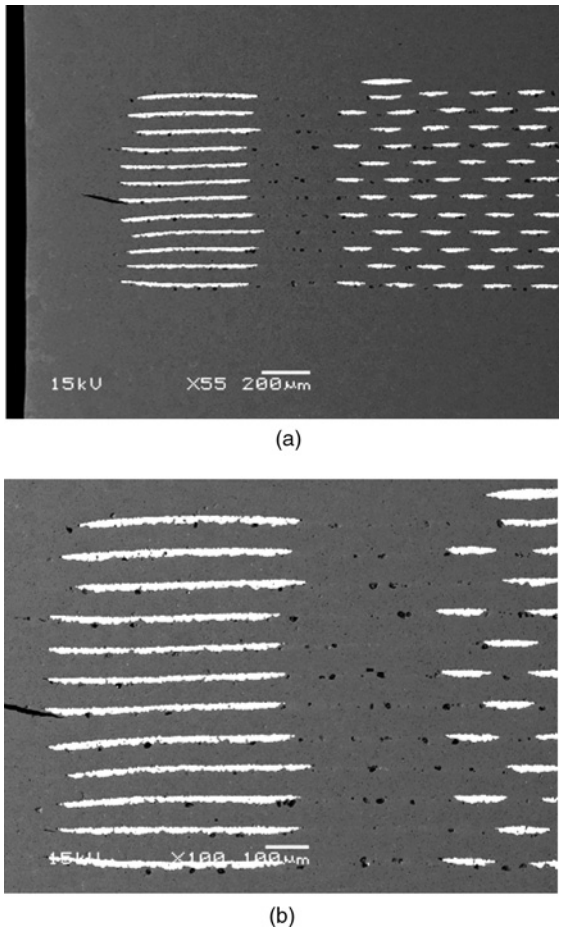

Fig. 23. SEM images of cross-sectioned D47 transformers from panel 1999Y at (a) low-magnification and (b) high-magnification. This panel of parts had a high-dielectric standoff between primary and secondary windings.

secondary windings reluctance and the center core reluctance. While increasing the number of gaps increases the center core reluctance, the reluctance of the secondary windings located inside the primary remains constant. Increasing the number of gaps will have little effect on this parallel reluctance combination once the center core reluctance exceeds the secondary winding reluctance. For the D48B design, the center core region possesses a cross-sectional area over three times smaller than the secondary windings region located inside the primary winding. Consequently, the center core region possesses a higher reluctance than the secondary windings region for the designs summarized in Table IV. This explains the relatively minor impact of the gap structure on inductance. Due to the small primary inductance variation, the designs all exhibited very comparable output voltage performance. Tests were also conducted that placed the dielectric gaps on different tape layers in the center core region, and similar results were obtained.

D. Impact of Endcap Structure on Performance

For the LTCC transformer design and construction, the tape layers placed above and beneath the windings layers—referred to as the endcap layers—present the lowest cross-sectional area to the flux generated by the primary winding. Consequently, the endcap layers play an important role on the dynamic saturation characteristics of these devices. To study the impact of the endcaps on design performance, two D50E transformer designs were built and characterized. Table V summarizes the construction and measured parameters for the two designs. Note that the only difference in the designs relates to the number of endcap layers used in the build, which is equal to the difference between the number of tape layers (L) and number of windings (N_W). The design with additional endcaps (panel 2149Y) possessed both higher coupling and higher inductance.

Fig. 18 shows the output voltage performance for both designs as a function of primary current, and Fig. 19 provides output voltage versus voltage switch stress for both designs. The design with additional endcap layers displays higher output voltage for a given current, and also provides a more linear relationship between output voltage and switch voltage stress. For the design with fewer endcap layers (2144Y), the output voltage versus switch voltage stress shows a similar slope at lower output voltages, but possesses a lower slope at higher voltage levels. This bend in the curve suggests a change to one or more of the variables contained in (8), in particular the effective turns ratio and the primary leakage inductance. This could result from an earlier onset of saturation for the design with fewer endcaps.

To better understand the observed differences, finite element modeling was utilized to investigate the dynamic saturation behavior of the D50E transformer. Fig. 20 shows a series of contour plots for the 2144Y transformer design with increasing primary current (note the scale has been adjusted to better illustrate regions of saturation). At 1.1 A, the model shows that the region of the endcap layers adjacent to the center core area possesses the highest magnetization level and is nearing saturation (note that the ferrite possesses a saturation magnetization of approximately 3200 G, or 0.32 T). When the current increases to 1.25 A the endcap regions located

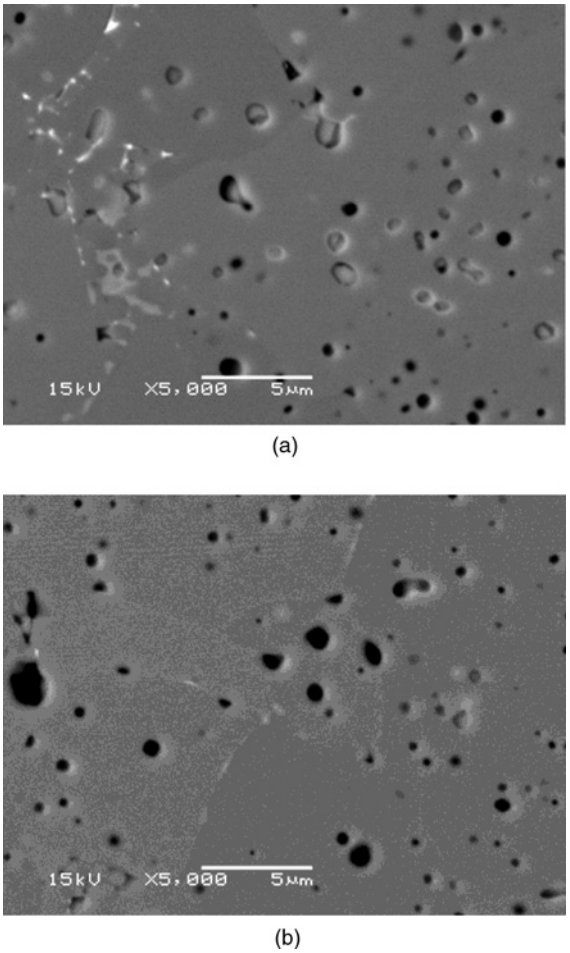

Fig. 24. SEM images of a D47 transformer from panel 1999Y at very high-magnification. (a) Image was taken in the low-permeability dielectric region between the primary and secondary windings. (b) Image was taken in a ferrite region away from the dielectric and conductor materials. The two images show a comparable level of porosity, suggesting the sintering behavior of the dielectric and ferrite materials are reasonably matched.

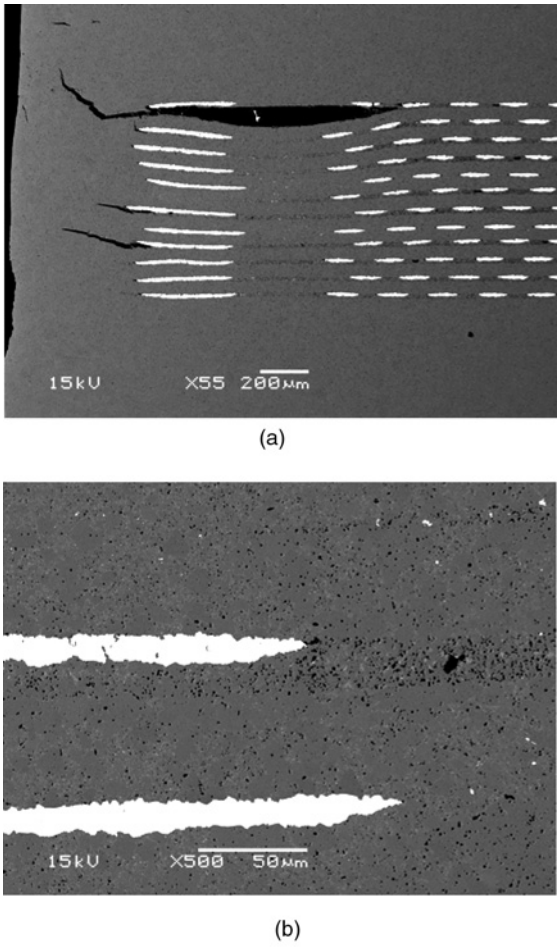

Fig. 25. SEM images of cross-sectioned D47 transformers from panel 2164Y at (a) low-magnification and (b) high-magnification. This panel of parts had a much lower dielectric standoff between primary and secondary windings relative to panel 1999Y. The images show a large void between primary and secondary windings that likely contributed to the reduced dielectric strength of this panel.

next to the center core become saturated. This onset of saturation between 1.1 A and 1.25 A agrees well with the observed bend in Fig. 19. With the endcap region next to the center core area saturated, more of the flux diverts through the secondary windings region located inside the primary winding. As a result, the endcap regions adjacent to the primary winding become more magnetized as the primary current continues to increase, and at 1.5 A the endcap regions above and below the primary become saturated. The level of saturation worsens for any further increase in the primary current.

The occurrence of saturation in the narrow endcap layers results in a soft saturation characteristic comparable to that observed with iron powder core materials. Consequently, although the output performance degrades the transformer continues to provide higher output voltage with increasing current. This soft saturation characteristic explains the different results shown in Fig. 19. The 2149Y parts, which possess a higher number of endcap layers, do not show evidence of saturation in Fig. 19. If the 2149Y parts were operated at increasing currents beyond those shown, their output voltage versus switch voltage stress would likely bend similar to 2144Y. Finally, note that the ratio of endcap layer thickness to center core radius determines whether saturation in the endcap layers limits performances. For example, as shown in Fig. 21, the D48B design saturates in the center core area and not the endcap regions due to its small core radius.

E. Impact of Gap Location on Coupling

The D47 transformer design, with all secondary windings located inside the primary winding, possesses very poor coupling (Table II). As discussed previously, the poor coupling results because the D47 transformer center core region possesses a net reluctance comparable to the reluctance of the magnetic path passing through the secondary windings region. As a result the flux shows little preference to traverse through the center core region instead of the windings region. Removing the gaps from the center core region significantly improves the coupling, providing a coupling coefficient k as high as 0.93 in D47 units built without any center core gaps. However, these designs provide poor output performance due to saturation at low-primary currents.

The introduction of the low-permeability gaps into the center core region for the D47 design negatively impacts coupling performance. One simple way to overcome this effect while still providing a high-saturation magnetizing current involves placing the low-permeability dielectric gaps along the edge of the part (i.e., in the edge margin), instead of in the center core. This keeps the reluctance of the center core region low compared to the secondary windings region, while keeping the net transformer reluctance large enough to avoid saturation at low-magnetizing currents. Fig. 22 shows an image comparing modeling results for two D47 designs with these different approaches to "gapping" the part. Based on the models, the D47 design with the gaps in the center core region possesses a coupling coefficient equal to 0.746 (which agrees well with the results in Table II); whereas the part containing gaps along the edge possesses a coupling coefficient of 0.923. Inserting the dielectric gaps on the edge of the parts provides a method for significantly improving coupling of this LTCC transformer design. Note that this approach provides little impact on the interleaved D48B and D50E designs since these designs have secondary windings located outside the primary windings. Additionally, it should be mentioned that the location of the low-permeability gaps in the edge margin will create flux external to the transformer along the edge of the part. This might limit its use in circuits with a high-sensitivity to electromagnetic interference.

F. Effect of Microstructure on Insulation Properties

For transformers that generate high-output voltages the primary–secondary insulation properties are critical. In order to achieve good insulation in the LTCC transformer, a void-free monolithic structure is desirable as well as cofired ferrite and dielectric materials with excellent dielectric standoff capability. Achieving a void-free monolithic structure requires highly compatible materials, closely matched sintering shrinkage and shrinkage rates between materials, and a well characterized and controlled sintering profile. Dielectric standoff testing on transformers from separate lots built using separate batches of material showed a large variation of the primary–secondary breakdown properties. To better understand these differences the samples were cross-sectioned, polished, and imaged using a scanning electron microscope (SEM) for analysis.

Fig. 23 shows SEM images for a cross-sectioned part from panel 1999Y, a D47 design with an average primary–secondary dielectric standoff of 3700 volt alternating current (VAC) rms (note that all dielectric standoff testing used a ramp rate of 500 VAC rms/s). In the image the bright regions correspond to the primary and secondary windings; the gray regions represent the ferrite and dielectric materials; and the regions of porosity are dark in contrast. The thin dielectric layers printed over the windings are barely visible in the images. Fig. 24 shows a higher magnification image of the region between the primary and secondary windings [Fig. 24(a)], as well as an image of a ferrite region removed from the windings region [Fig. 24(b)]. As shown in Figs. 23 and 24, the scale of the porosity in the dielectric between the primary and secondary windings appears comparable to the

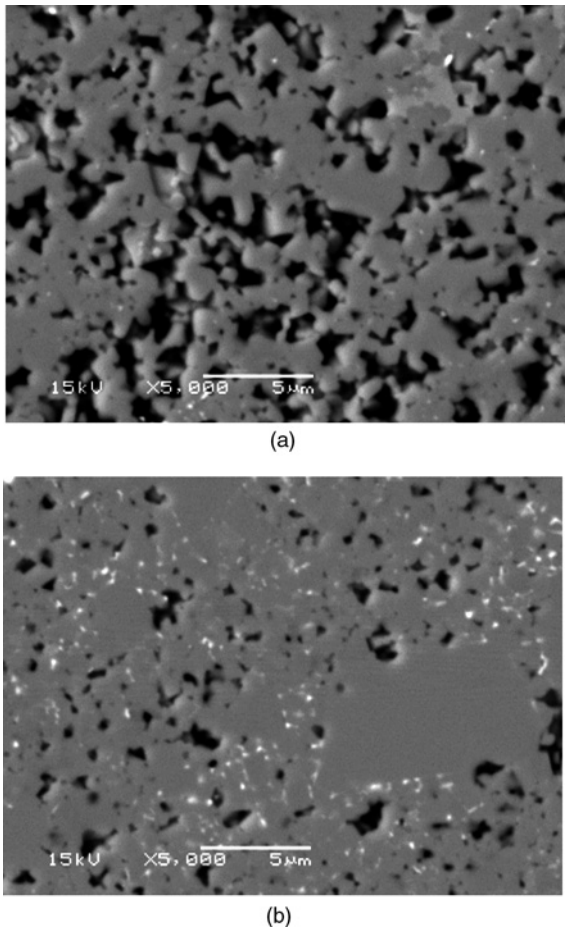

Fig. 26. SEM images of a D47 transformer from panel 2164Y at very high-magnification. (a) Image was taken in the low-permeability dielectric region between the primary and secondary windings. (b) Image was taken in a ferrite region away from the dielectric and conductor materials. The two images show markedly different levels of porosity, suggesting the dielectric and ferrite materials possessed a poorly matched shrinkage rate when sintered.

porosity in the ferrite regions. This suggests the dielectric and ferrite materials possessed a reasonably matched sintering shrinkage/rate, which helps produce a monolithic structure. However, compared to the solid, monolithic structure that surrounds the (central) transformer region, there is visibly more porosity between the tape layers within the transformer edge margin region (Fig. 23). This porosity indicates that there are some materials and or processing incompatibilities in the system that could possibly be optimized. Nonetheless, the high-dielectric standoff voltage for these parts indicates that small pores isolated between dense regions may be tolerable.

Fig. 25 shows SEM cross-section images from panel 2164Y, which used a different batch of dielectric material for its build. These transformers possessed a much lower breakdown voltage of 2100 VAC rms between the primary and secondary. The cross-sections showed large voids present between the primary and secondary windings, which undoubtedly contributed to the reduced dielectric standoff of these parts. These large voids may result from gas buildup in the part during the organic binder removal process, from stresses created due to a mismatch in shrinkage or the rate of shrinkage between the dielectric and ferrite materials, or from stresses created

during the lamination process. In addition, the dielectric layer possessed a much higher level of porosity than the ferrite (Fig. 26). This also suggests a shrinkage mismatch between the dielectric and ferrite materials used for this panel, which likely resulted in poor densification of the low-permeability dielectric material. The images shown in Figs. 23–26 illustrate the importance of the material shrinkage and sintering characteristics on the final transformer microstructure and its impact on the dielectric standoff properties of the sintered device.

VII. Conclusion

This paper discussed the application of LTCC transformers for generating high voltages using a flyback converter topology. The LTCC transformers possess a monolithic structure with the coils surrounded by ferrite material, which in general leads to poor coupling for these designs. Despite the relatively poor coupling, multiple transformer designs achieved output voltages in excess of 2 kV. Several methods for improving the coupling in these devices were identified, which includes interleaving the primary, locating the gaps on the edge instead of the center of the part, increasing the number of winding layers in the design, and increasing the number of endcap layers when saturation in the endcap layers limits performance. Finally, analysis of cross-sectioned transformers highlighted primary–secondary dielectric standoff issues that result when the lamination and sintering operations produce a poor microstructure. Overall, these devices look promising for applications that need to convert a low-input voltage to output voltages up to several kilovolts.

References

[1] S. Chenetz, "Photoflash high-voltage power supply," Micrel Application Note 20 [Online]. Available: http://www.micrel.com/_PDF/AppNotes/an-20.pdf

[2] C. Quinn, K. Rinne, T. O'Donnell, M. Duffy, and C. O. Mathuna, "A review of planar magnetic techniques and technologies," in *Proc. 16th Annu. IEEE Appl. Power Electron. Conf. Expo. (APEC)*, vol. 2. Mar. 2001, pp. 1175–1183.

[3] E. Waffenschmidt, "Design and application of thin, planar magnetic components for embedded passives integrated circuits," in *Proc. IEEE 35th Annu. IEEE Power Electronics Specialists Conf.*, vol. 6. Jun. 2004, pp. 4546–4552.

[4] "Snubber circuits suppress voltage transient spikes in multiple output dc–dc flyback converter power supplies," Maxim Application Note 848 [Online]. Available: http://www.maxim-ic.com/an848

[5] D. A. Abel, "Multi-layer transformer apparatus and method," U.S. Patent 6 198 374, March 6, 2001.

[6] R. L. Wahlers, C. Y. D. Huang, M. R. Heinz, A. H. Feingold, J. Bielawski, and G. Slama, "Low-profile LTCC transformers," in *Proc. Int. Microelectron. Packag. Soc. Conf.*, vol. 4931. 2002, pp. 76–80.

[7] G. Slama, "Low-temperature cofired magnetic tape yields high benefits," *Power Electron. Technol.*, vol. 29, no. 1, pp. 30–34, Jan. 2003.

[8] D. C. Meeker. (2006, Dec. 3). *Finite Element Method Magnetics*, Version 4.0.1 [Online]. Available: http://femm.foster-miller.net

Alexander W. Roesler photograph and biography not available at the time of publication.

Joshua M. Schare photograph and biography not available at the time of publication.

S. Jill Glass photograph and biography not available at the time of publication.

Kevin G. Ewsuk photograph and biography not available at the time of publication.

George Slama photograph and biography not available at the time of publication.

David Abel photograph and biography not available at the time of publication.

Daryl Schofield photograph and biography not available at the time of publication.